DOI 10.5162/Ultrasonic2025/B1-b1

Passive Cavitation Mapping of Focused Ultrasound Induced Cavitation on Magnetic Nanoparticles

Christian Marinus Huber[1,2,*], *Helmut Ermert*[1], *Ingrid Ullmann*[2], *Martin Vossiek*[2], *and Stefan Lyer*[1]

[1] *Department of Otorhinolaryngology, Head and Neck Surgery, Section of Experimental Oncology and Nanomedicine (SEON), Professorship for AI-Controlled Nanomaterials (KINAM), Universitätsklinikum Erlangen, Glücksstrasse 10a, Erlangen, 91054, Bavaria, Germany*

[2] *Institute of Microwaves and Photonics (LHFT), Friedrich-Alexander-Universität Erlangen-Nürnberg, Cauerstrasse 9, Erlan-gen, 91058, Bavaria, Germany*

[*] *Christian.Ch.Huber@fau.de*

Abstract: Magnetic nanoparticles (MNPs) are utilized in Magnetic Drug Targeting (MDT) to treat tumors, for which it would be advantageous to develop a monitoring method. We aim to use the cavitation produced by MNPs in a focused ultrasonic (FUS) field for imaging via passive cavitation mapping (PCM), a novel approach for MNP mapping. MNP-PCM has the advantage of real-time imaging capability and compatibility with flow conditions over other MNP imaging modalities. Additionally, cavitation can enhance perfusion and drug release. We demonstrate a PCM system for MNPs using time domain Delay and Sum (DAS); Delay Multiply and Sum (DMAS); and the Robust Capon Beamforming (RCB). The code used is available at github.com/ChristianHuber555/ICU_MNP_PAM.

Keywords: Ultrasound Imaging, Magnetic Nanoparticles, Drug Delivery, Passive Imaging, Beamforming, Cavitation

Introduction

Nanomaterials are increasingly integrated into modern medicine for targeted therapy, diagnostics, or drug delivery [1]. Notably, lipid-based nanoparticles were employed in mRNA COVID-19 vaccines [2], highlighting the translational impact of nanoscale systems. Other nanocarriers—such as polymeric, gold, and magnetic nanoparticles (MNPs)—enable a broad range of biomedical applications, including tissue engineering, molecular imaging, and cancer therapy. MNPs offer unique advantages due to their responsiveness to external magnetic fields [3]. They are widely investigated for localized cancer treatments such as magnetic drug targeting (MDT) and magnetic hyperthermia [4]. In MDT, MNPs are accumulated magnetically to tumor regions, enabling site-specific chemotherapy. However, a critical limitation of this approach is the lack of real-time monitoring to assess particle distribution and treatment progression under physiological flow.

Ultrasound-based methods for imaging MNPs [5] have shown promise in MDT monitoring. However, most are inadequate for detecting MNPs in motion within vascular systems. In our previous work [6], [7], we demonstrated that lauric acid-coated MNPs (LA-MNPs) exhibit sonosensitivity, acting as cavitation nuclei under focused ultrasound (FUS). Cavitation is defined as the formation and dynamics of gas-filled bubbles and occurs as either stable cavitation (oscillatory behavior near equilibrium) or inertial cavitation (violent collapse). Acoustic cavitation enhances drug delivery through increased vascular permeability, localized drug release, and improved imaging contrast [8]. Cavitation can be used for imaging either by using the generated bubbles as high echogenic contrast in active cavitation mapping [9] or using acoustic cavitation emission in passive cavitation mapping (PCM) [10].

In this study, we utilize the sonosensitivity of our LA-MNPs to induce inertial cavitation under flow and apply PCM to map their spatial distribution. This approach has the potential to enable real-time monitoring of MNP transport during MDT, providing a foundation for ultrasound-guided, feedback-controlled nanoparticle therapy.

Methods and Materials

In time-domain Passive Cavitation Mapping (PCM) [10], the cavitation intensity at each spatial location $\mathbf{x} = (x, z)^T$ is quantified by integrating the squared source strength $q(\mathbf{x}, t)$ over a temporal window T

$$I(\mathbf{x}) = \frac{1}{\rho c} \int_{t_0}^{t_0+T} q(\mathbf{x}, t)^2 \mathrm{d}t, \tag{1}$$

where ρ is the density of the medium and c is the speed of sound.

The accuracy of PCM critically depends on the beamforming algorithm used to reconstruct $q(\mathbf{x}, t)$

and $I(\mathbf{x})$. In this work, we evaluate and compare the conventional Delay-and-Sum (DAS) beamformer [10], the non-linear Delay-Multiply-and-Sum (DMAS) beamformer [11], and the statistically adaptive Robust Capon Beamformer (RCB) [12]. Each method offers distinct trade-offs in resolution, robustness to noise, and sensitivity to cavitation signals.

For all beamforming methods, cavitation emissions must be passively recorded using multiple spatially distributed sensors—typically a linear array transducer. The positions of the N transducer elements are denoted as $\mathbf{x}_n = (x_n, z_n)^T = (x_n, 0)$, with received signals $s_n(t)$ for each element $n \in \mathcal{N}$, $1 \leq n \leq N$. As the acquisition is restricted to 2D imaging, the out-of-plane y-axis is neglected and set to $y = 0$ throughout all computations.

For a target location $\mathbf{x}$, the geometric distance between the pixel and each sensor element is given by

$$d_n(\mathbf{x}) = \sqrt{z^2 + (x_n - x)^2}. \tag{2}$$

Eq. (2) defines the propagation distance from each pixel to sensor n, and the corresponding time delay is $\tau(\mathbf{x}) = d_n(\mathbf{x})/c$. The DAS beamformer estimates the source strength by

$$q_{\mathsf{DAS}}(\mathbf{x}, t) = \frac{1}{N\alpha} \sum_{n=1}^{N} s_n(t + \tau_n(\mathbf{x})), \tag{3}$$

where α is the piezoelectric sensitivity coefficient of the array elements. The DMAS beamformer extends DAS by introducing pairwise nonlinear correlations

$$q_{\mathsf{DMAS}}(\mathbf{x}, t) = \frac{1}{(N^2 - N)\alpha} \sum_{n_1=1}^{N-1} \sum_{n_2=n_1+1}^{N} \widehat{s}_{n_1} \widehat{s}_{n_2}, \tag{4}$$

where the modified signal is defined as $\widehat{s}_n = \mathrm{sign}\{s_n(t)\} \cdot \sqrt{|s_n(t)|}$. To reduce computational complexity, Eq. (4) can be reformulated

$$q_{\mathsf{DMAS}}(\mathbf{x}, t) = \frac{1}{N(N-1)\alpha} \frac{e_1^2 - e_2}{2} \tag{5}$$

using power sums

$$e_j = \sum_{n=1}^{N} \widehat{s}_n^j. \tag{6}$$

To compute the cavitation intensity map using RCB the received signals are ordered to a vector

$$\mathbf{s}(\mathbf{x}, t) = \begin{bmatrix} s_1(t - \tau_1(\mathbf{x})) \\ \vdots \\ s_N(t - \tau_N(\mathbf{x})) \end{bmatrix}. \tag{7}$$

RCB is a statistically optimal beamforming approach that minimizes the total output power while constraining the beamformer weights $\mathbf{w}$ to remain close to a unity gain response. The beamforming weights are obtained by solving the constrained optimization problem

$$\min_{\mathbf{w}} \{\mathbf{w}^T \mathbf{R}_S(\mathbf{x})^{-1} \mathbf{w}\} \quad \text{subject to} \quad \|\mathbf{w} - \mathbf{1} \leq \epsilon\| \tag{8}$$

where $\mathbf{R}_S(\mathbf{x}) = \mathbf{U}\mathbf{V}\mathbf{U}^T$ is the eigenvalue decomposition of the sample covariance matrix, $\mathbf{1}$ is a all-ones vector, and ϵ is a user-defined robustness parameter. The solution of Eq. (8) yields the beamforming weights used to compute the cavitation intensity

$$I(\mathbf{x}) = \frac{1}{\alpha^2 \rho c} \frac{1}{\widehat{\mathbf{a}}_0 \mathbf{U}\mathbf{V}(\lambda^2 \mathbf{I} + 2\lambda^{-1}\mathbf{V} + \mathbf{V}^2)^{-1}\mathbf{U}^T \widehat{\mathbf{a}}_0}, \tag{9}$$

with $\mathbf{I}$ as an all-ones matrix, λ as Lagrange multiplied and $\widehat{\mathbf{a}}_0 = \widehat{\mathbf{a}}N/\|\widehat{\mathbf{a}}\|$ with $\widehat{\mathbf{a}} = \mathbf{1} - \mathbf{U}(\mathbf{I} + \lambda\mathbf{V})^{-1}\mathbf{1}$. The Lagrange multiplier can be found by solving

$$\|(\mathbf{I} + \lambda \mathbf{R}_S^{-1}\mathbf{1})\| - \epsilon = 0. \tag{10}$$

The experimental setup is illustrated in Fig. 1. A tissue-mimicking phantom containing a 2 mm diameter flow channel was fabricated from 2 wt% agarose, 1 wt% silica gel, and 97 wt% ultrapure water, following the procedure described in [13]. The flow channel was aligned with the focal region of a focused ultrasound (FUS) field (center frequency $f = 835$ kHz, pulse duration $t_{\mathsf{on}} = 200$ μs, mechanical index = 1, 10 pulses per acquisition).

A suspension of LA-MNPs at a concentration of 3 mg Fe/mL was circulated through the channel. Cavitation emissions were passively captured using 64-elements of the 128 element linear array transducer (Verasonics 64 LE, L11-5v; center frequency 7.6 MHz, relative bandwidth 77%) positioned orthogonally to the FUS propagation axis and mounted above the phantom.

Signals were recorded at a sampling rate of 31.25 MHz and subsequently upsampled to 55.11 MHz. A comb notch filter was applied to suppress the FUS fundamental and harmonic frequencies. The preprocessed array signals were reconstructed using the DAS, the DMAS, and the RCB. Cavitation intensity maps were computed and averaged over all 10 FUS pulses. For quantitative evaluation, the contrast ratio (CR) between cavitating and non-cavitating regions was used.

Results and Discussion

Using the described setup, cavitation on magnetic nanoparticles was successfully induced via focused

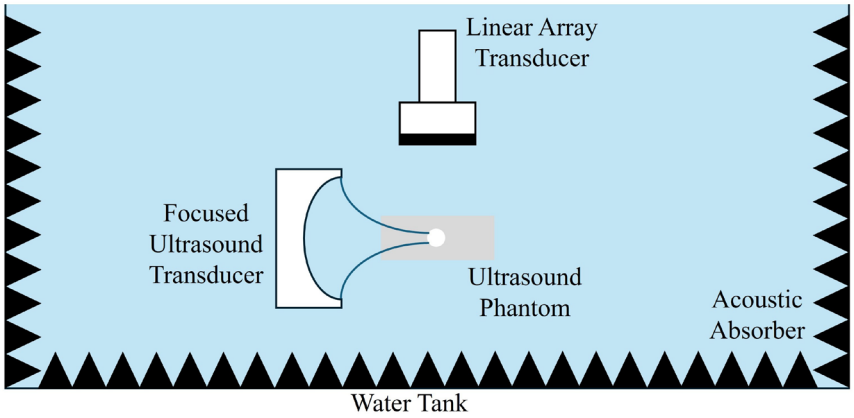

Fig. 1: Measurement setup used for passive cavitation mapping of focused ultrasound induced cavitation on magnetic nanoparticles.

ultrasound. The resulting acoustic emissions were passively received by the linear array transducer and processed using DAS, DMAS, and RCB beamforming algorithms. The reconstructed cavitation maps are shown in Fig. 2.

All beamformers were able to localize cavitation activity within the phantom. However, notable differences in spatial specificity and artifact suppression were observed. The DAS reconstruction shows widespread intensity outside the flow channel, indicating poor spatial confinement. In contrast, RCB provides improved localization, effectively suppressing off-target signal but introducing artifacts near the bottom boundary of the phantom, likely due to reflections. DMAS offers a balance between spatial resolution and artifact suppression, producing a confined cavitation region without the lower-edge artifacts seen in RCB.

Quantitatively, the contrast ratio was used to evaluate performance: DAS yielded a CR of -7.79 dB, RCB -7.17 dB, and DMAS - 5.91 dB. Among the three, DMAS demonstrated the best overall performance in terms of both CR and artifact-free localization.

These results confirm that passive cavitation mapping can effectively visualize FUS-induced cavitation on MNPs under flow conditions, and that DMAS offers the most robust imaging performance in this context.

Conclusion

This study demonstrates the feasibility of using PCM to monitor FUS-induced cavitation on MNPs under flow conditions. By utilizing the sonosensitive properties of LA-coated MNPs, we enabled cavitation-based imaging that can be used for real-time monitoring of MDT.

The DAS, DMAS, and RCB were evaluated for their ability to reconstruct MNP-cavitation intensity maps from passively received acoustic signals. While all methods successfully localized cavitation activity, DMAS provided the best balance of contrast, spatial confinement, and artifact suppression, achieving the highest CR. RCB improved localization but exhibited boundary artifacts, whereas DAS was limited by poor spatial resolution.

These findings demonstrate PCM as a promising tool for real-time, non-invasive monitoring of MNP transport during MDT. Future work will focus on in vivo validation, optimization for 3D imaging, and integration with feedback control systems for image-guided therapy.

Acknowledgments

The authors gratefully acknowledge the financial support of the German Research Foundation (DFG) - project number 452821018, and the Julitta und Richard Müller Stiftung.

References

[1] J. Damodharan, 'Nanomaterials in medicine – an overview,' *Materials Today: Proceedings*, vol. 37, pp. 383–385, 2021. DOI: 10.1016/j.matpr.2020.05.380.

[2] R. S. Shapiro, 'Covid-19 vaccines and nanomedicine,' *International Journal of Dermatology*, vol. 60, no. 9, pp. 1047–1052, 2021. DOI: 10.1111/ijd.15673.

[3] A. S. Thalmayer, K. Götz, M. Lübke and G. Fischer, 'Experimental and simulative analysis of magnetic nanoparticle accumulation using various halbach arrays,' *Current Directions in Biomedical Engineering*, vol. 10, no. 4, pp. 649–652, 2024. DOI: 10.1515/cdbme-2024-2159.

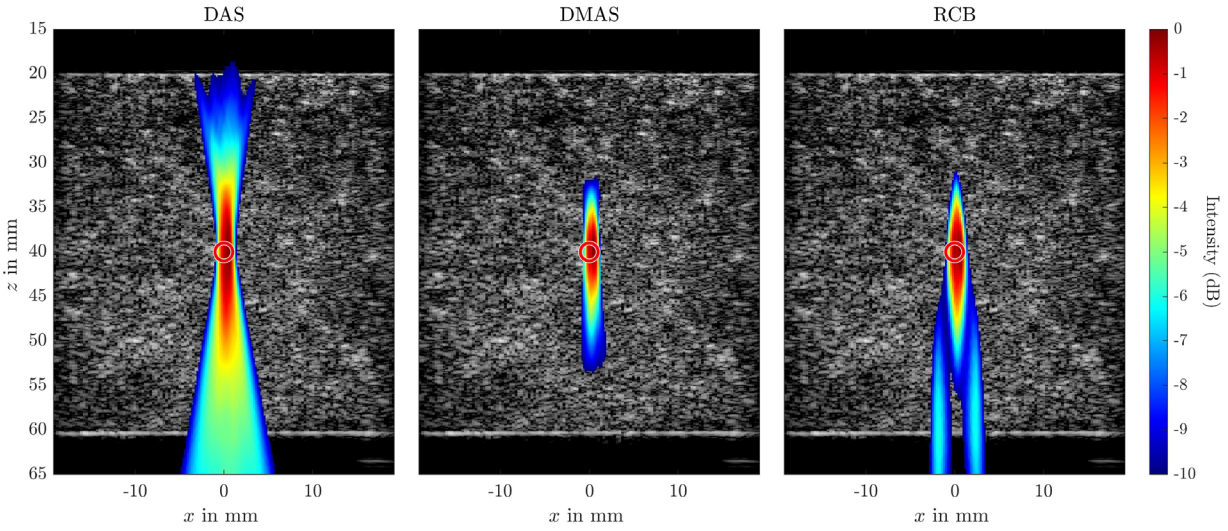

Fig. 2: Resulting cavitation intensity maps overlaid on the B-mode image using the Delay and Sum (DAS), Delay Multiply and Sum (DMAS), and Robust Capon Beamformer (RCB). $\epsilon = 10$ *was used for the RCB. The flow channel is shown as red circle in each plot.*

[4] R. Tietze et al., 'Efficient drug-delivery using magnetic nanoparticles–biodistribution and therapeutic effects in tumour bearing rabbits,' *Nanomedicine : Nanotechnology, Biology, and Medicine*, vol. 9, no. 7, pp. 961–971, 2013. DOI: 10.1016/j.nano.2013.05.001.

[5] C. M. Huber et al., 'A review on ultrasound-based methods to image the distribution of magnetic nanoparticles in biomedical applications,' *Ultrasound in Medicine & Biology*, vol. 51, no. 2, pp. 210–234, 2025. DOI: 10.1016/j.ultrasmedbio.2024.10.007.

[6] C. Huber et al., 'Ultrasound-mediated cavitation of magnetic nanoparticles for drug delivery applications,' *Current Directions in Biomedical Engineering*, vol. 8, no. 2, pp. 568–571, 2022. DOI: 10.1515/cdbme-2022-1145.

[7] C. M. Huber et al., 'Ultrasound-induced stable and inertial cavitation of magnetic nanoparticles for drug delivery applications,' *Current Directions in Biomedical Engineering*, vol. 10, no. 4, pp. 328–331, 2024. DOI: 10.1515/cdbme-2024-2080.

[8] Z. Shen, J. Shao, J. Zhang and W. Qu, 'Ultrasound cavitation enhanced chemotherapy: In vivo research and clinical application,' *Experimental Biology and Medicine (Maywood, N.J.)*, vol. 245, no. 14, pp. 1200–1212, 2020. DOI: 10.1177/1535370220936150.

[9] T. Ding et al., 'Spatial-temporal three-dimensional ultrasound plane-by-plane active cavitation mapping for high-intensity focused ultrasound in free field and pulsatile flow,' *Ultrasonics*, vol. 69, pp. 166–181, 2016. DOI: 10.1016/j.ultras.2016.04.010.

[10] M. Gyöngy and C.-C. Coussios, 'Passive spatial mapping of inertial cavitation during hifu exposure,' *IEEE Transactions on Biomedical Engineering*, vol. 57, no. 1, pp. 48–56, 2010. DOI: 10.1109/TBME.2009.2026907.

[11] S. Lu, R. Li, X. Yu, D. Wang and M. Wan, 'Delay multiply and sum beamforming method applied to enhance linear-array passive acoustic mapping of ultrasound cavitation,' *Medical Physics*, vol. 46, no. 10, pp. 4441–4454, 2019. DOI: 10.1002/mp.13714.

[12] C. Coviello et al., 'Passive acoustic mapping utilizing optimal beamforming in ultrasound therapy monitoring,' *The Journal of the Acoustical Society of America*, vol. 137, no. 5, pp. 2573–2585, 2015. DOI: 10.1121/1.4916694.

[13] C. M. Huber, N. Dorsch, H. Ermert, M. Vossiek, I. Ullmann and S. Lyer, 'Passive cavitation mapping for biomedical applications using higher order delay multiply and sum beamformer with linear complexity,' *Ultrasonics*, vol. 153, p. 107 653, 2025. DOI: 10.1016/j.ultras.2025.107653.